Available online at www.sciencedirect.com
ScienceDirect
Journal of the European Ceramic Society 29 (2009) 391–401
www.elsevier.com/locate/jeurceramsoc

Fabrication of yttria-stabilized-zirconia thick coatings via slurry process with pressure infiltration

Weihua Lan, Ping Xiao *

School of Materials, University of Manchester, Manchester M1 7HS, UK

Received 26 February 2008; received in revised form 21 April 2008; accepted 25 May 2008
Available online 26 July 2008

Abstract

Yttria-stabilized-zirconia (YSZ) coatings with thicknesses up to 420 μm have been prepared using a novel slurry process with pressure infiltration. Binary-sized particle slurries (binary-slurries), composed of nano-particle slurry (nano-slurry) and micro-sized preformed particles, were cast on metal substrates to form coatings. After sintering at 1150 °C for 1 h, preformed particles were cemented with nano-particles to form a porous YSZ coating. Subsequently, the nano-slurry was infiltrated into the porous coatings under pressure. The infiltrated nano-slurry filled the pores, and was sintered together with the porous coating, resulting in an increase in both density and mechanical properties of the coating. After 5–6 infiltration cycles, the coating reached 82% theoretic density and micro-hardness of 3.7 GPa. Such coatings could be used as thermal barrier coatings for high temperature applications.

Keywords: Nano-slurry; Coating; Infiltration; Density; Hardness; YSZ

1. Introduction

Suspensions/slurries, prepared by dispersing sub-micrometer ceramic particles in liquid, have been applied on metal substrates to form ceramic coatings in the past decades.[1,2] During drying and sintering, the coating shrinks at the thickness direction while the coating plane is constrained by the substrate. Tensile stresses arise due to the constrained volume shrinkage, resulting in high porosity[3] and leading to warping,[4] cracking even delamination.[5] For drying, large particle size is desirable to decrease the tensile stress which scales with the capillary pressure applied by the liquid in pores of a wet coating.[2,6,7] For sintering, Garino and Bowen proved that cracks were less likely to occur in coatings where a viscous sintering mechanism dominated, in comparison with the case of solid-state crystalline sintering.[8] In a viscous sintering process, the magnitude of constrained stresses is dependent on the ratio between the shear rate ($\dot{\varepsilon}_s \propto R_P^{-2}$, R_p is the particle size) and the densification rate ($\dot{\varepsilon}_d \propto R_P^{-3}$) of a coating.[9] Therefore, increasing particle size will reduce the constrained stresses in both drying and sintering processes. However, larger particles have lower sintering potential than smaller particles, thus requiring a higher sintering temperature.[10]

In order to balance the effect of particle size on constrained tensile stresses and sintering potential, a novel slurry method, referred to as the 'mortar-bricks' approach, has been proposed by our group.[7,11] Binary-slurries were first prepared by mixing micro-particles and nano-slurries, and then were applied on metal substrates to form wet coatings. In the blending process, nano-particles were adhered to the surfaces of micro-particles, resulting in the lower viscosity and higher solid content of such binary-slurry compared to the original nano-slurry, which is beneficial for slurry coating. During drying, the micro-particles, which were embedded in the nano-slurry, worked as 'bricks' and effectively reduced tensile stresses and prevented crack formation.[7] The sintering of such coatings is expected to take advantage of the low sintering temperature of nano-particles which accumulate at the surfaces of micro-particles and cement micro-particles as 'mortar', while allows the micro-particles to form a skeleton structure and maintain the coating integrity.

One drawback of the coatings prepared using the 'mortar-bricks' approach is the highly porous microstructure, which compromises some coating properties and performances, such as hardness, wear/erosion resistance.[11] Pressure infiltration, which has been successfully used to prepare dense packing of particles

* Corresponding author.
E-mail address: ping.xiao@manchester.ac.uk (P. Xiao).

0955-2219/$ – see front matter © 2008 Elsevier Ltd. All rights reserved.
doi:10.1016/j.jeurceramsoc.2008.05.052

inside a fibre preform,[12–15] provides a possibility to improve the density of porous coatings. As long as the pores are interconnected in a sintered coating, a particle suspension can be infiltrated into the coating under an applied pressure. Thereafter, infiltrated ceramic particles can consolidate inside the porous structure to fill open pores and decrease the porosity. The infiltration dynamics are determined primarily by the pore structure of the preform, and the particle size distribution, physicochemical, hydrodynamic properties of the infiltrated suspension.

Understanding the sintering mechanism of such coatings composed of binary-sized particles and the evolution of the coating structure with infiltration is crucial to develop the 'mortar-bricks' approach further to fabricate thick and dense ceramic coatings, which has the potential to be used as thermal barrier coatings (TBCs). In this paper, porous yttria-stabilized-zirconia (YSZ) coatings were first prepared using the 'mortar-bricks' approach. Subsequently, the coatings, which had been sintered at 1150 °C for 1 h, were repeatedly infiltrated with a nano-slurry. The effect of infiltration on coating microstructure and mechanical properties has been examined. Meanwhile, the infiltration process was discussed based on the Darcy's law.

2. Experimental procedure

2.1. Materials

An aqueous YSZ nano-particle slurry (MEL Chemicals, Manchester, UK) was used as a starting material, which is with composition of 8 wt% Y_2O_3–ZrO_2, solid concentration of 4 vol%, and primary particle size of 12 nm. The pH value of the as-received nano-slurry was adjusted in the range of 1.5–12 by the addition of dilute hydrochloric acid (HCl) or sodium hydroxide (NaOH) with continuous magnetic stirring. After 24 h stirring, the pH-modified nano-slurries were concentrated to a high solid content of 4–18.6 vol% by air drying at room temperature. The concentrated nano-slurries were used for coating fabrication and infiltration experiments.

2.2. Fabrication of porous YSZ coatings

Fig. 1 shows the flowchart of coating fabrication used in this study. Micro-sized irregularly shaped preformed particles were prepared as follows. The nano-slurry with a pH 1.5 was dried into solid compacts in an ambient environment. The solid compacts were ground into irregularly shaped particles using an agate mortar, and were sieved using a screen. The sieved particles were sintered at 1150 °C for 1 h, followed by another round of grinding and sieving. Two types of preformed particles were prepared using the sieves with a mesh size of 45 and 75 μm, respectively.

YSZ binary-slurries were prepared by mixing preformed particles and a nano-slurry with pH 1.5 and 11.5 vol% solid content which was sufficiently viscous to prevent segregation or sedimentation of the preformed particles. The weight ratio of preformed particles to nano-particles (recorded as $R_{M/N}$) was controlled at 5/1 based on previous results which showed the binary-slurries with $R_{M/N} = 5/1$ could be used to prepare uncracked green coatings with a thickness >300 μm.[7] In this study, YSZ coatings were prepared by casting the binary-slurries on Fecralloy substrates in a square shape (10 mm × 10 mm) and with a wet coating thickness of around 600 μm. During drying in an ambient environment, the thickness reduction of wet coatings was measured using a calibrated optical microscope (Olympus BH, Tokyo, Japan), and the thickness shrinkage was calculated as the measured thickness reduction over the initial coating thickness. The green density was calculated as weight/volume. After drying, the green coatings were heated at 5 °C/min to 1150 °C and hold for 1 h, thereafter cooled at 5 °C/min to room temperature. The sintered coatings were infiltrated with a nano-slurry.

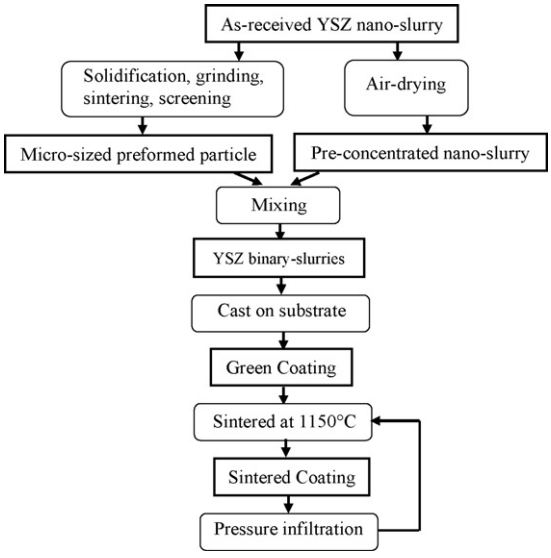

Fig. 1. Flowchart of coating preparation via slurry process and pressure infiltration.

2.3. Pressure infiltration

A customer-built pressure infiltration apparatus was used for infiltration experiments. This apparatus consists of a vacuum chamber which is connected to a vacuum pump and a pressure bottle, as schematically shown in Fig. 2. Nano-slurries with pH in the range of 1.5–7.5 and solid content in the range of 4–18.6 vol% were used as infiltrated slurries to investigate the effect of slurry properties on infiltration. A layer, with ~2 mm thickness, of the infiltrated nano-slurry was spread on the top surface of a sintered coating which was placed in the vacuum chamber and the vacuum chamber was evacuated. When the vac-

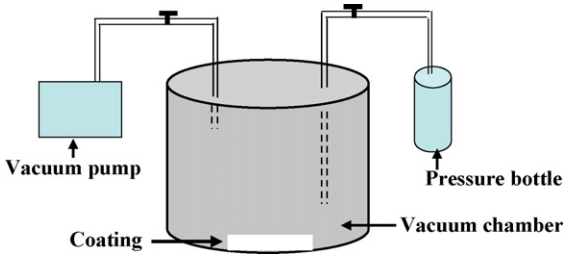

Fig. 2. Schematic of the pressure infiltration apparatus.

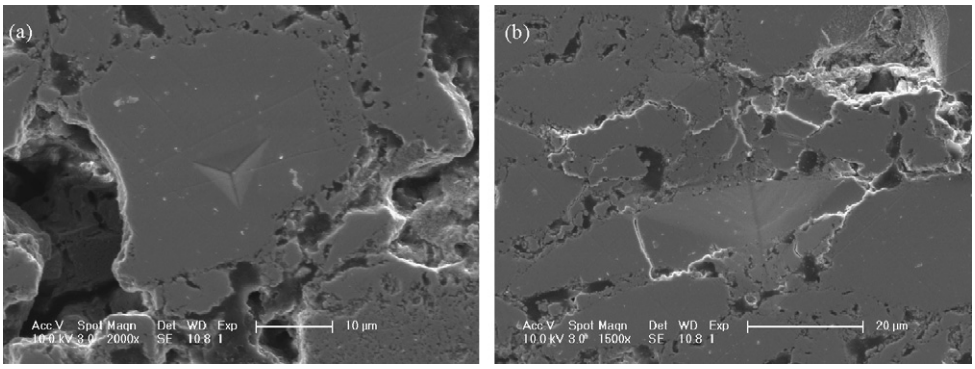

Fig. 3. SEM micrograph of (a) a typical nano-indent on preformed particles and (b) a typical micro-indent covering both preformed particles and nano-particles.

uum reached 70 Pa, the vacuum valve was closed and a pressure was applied gradually up to 100 MPa and remained at 100 MPa for 60 s. Under this pressure, the slurry should be infiltrated into the porous coating. After infiltration, the residual slurry which still remained as fluid regardless of water evaporation during evacuation was removed from the top surface of the coating which, then, was dried in an ambient environment overnight, followed by sintering at 1150 °C for 1 h. The coatings were repeatedly infiltrated, dried, and sintered for 5–6 times to achieve a high density. Such a cycle of infiltration-drying-sintering was referred to as an infiltration cycle.

2.4. Characterization of nano-slurries

The zeta potential of YSZ nano-particles was measured in diluted nano-slurries using a doppler electrophoretic light scattering analyzer (Beckman, Coulter DELSA 440SX, Miami, Florida, USA). The viscosity of nano-slurries was measured as a function of the pH value and solid content using a cone-plate viscometer (Brookfield, VIII-Rhometer, Essex, UK). Particle/agglomerate size distributions were measured using a Microtrac particle size analyzer (Malvern, Micro Trac ×100, Worcestershire, UK).

2.5. Characterization of coatings

The morphology of preformed particles and the cross section of sintered coatings were examined using a Field Emission Gun scanning electron microscope (FEG-SEM, Philips XL-30, Eindhoven, The Netherlands). The pore structure and open porosity of coatings after removal of the metal substrate with dissolution in $HCl + HNO_3$ solution were measured using a mercury intrusion technique (Quantachrome Poremaster, Hook, UK). The density of sintered coatings was approximately calculated by:

$$\rho_0 = 6.05(1 - P) \tag{1}$$

where P is the open porosity of a sintered coating measured using the mercury intrusion method and 6.05 g/cm^3 is taken as the theoretical density of YSZ particles. The sintering shrinkage was calculated as the difference between the sintered density and green density over the sintered density.

The weights of coatings were measured using a weight balance (Ohaus AB-S, Leicester, UK) which has a sensitivity of 0.01 mg. The relative weight gain, $W\%$, after an infiltration cycle was calculated by:

$$W\% = \frac{M_S - M_I}{M_I} \times 100\% \tag{2}$$

where M_I and M_S are the weights of a coating before and after an infiltration cycle. The density of infiltrated coatings was calculated by:

$$\rho = \rho_0(1 + W\%) \tag{3}$$

where ρ_0 is the density of a sintered coating without infiltration which can be calculated using Eq. (1).

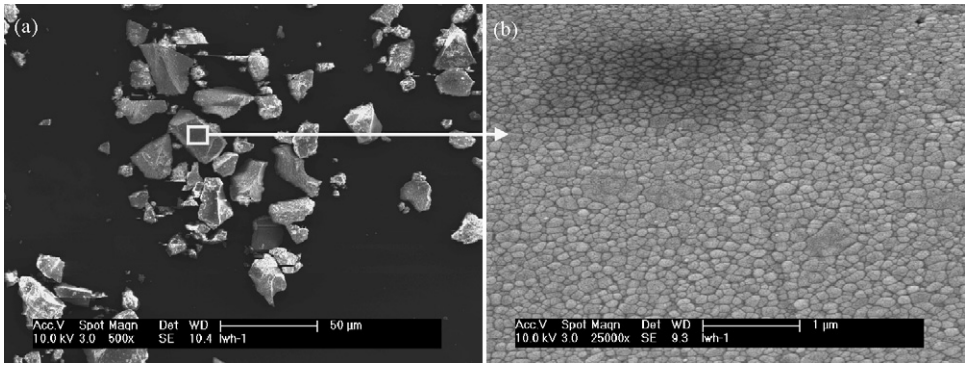

Fig. 4. (a) SEM micrograph of irregularly shaped preformed particles and (b) nano-crystalline microstructure of preformed particles.

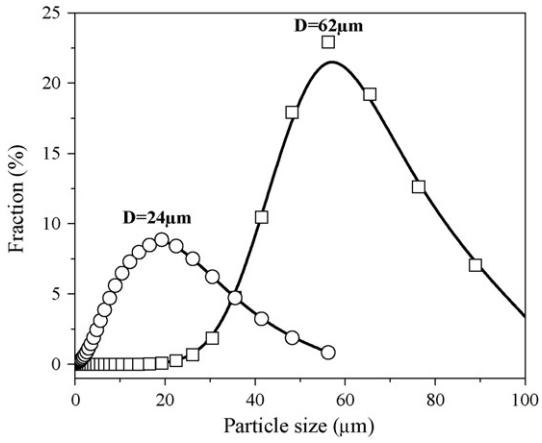

Fig. 5. Particle size distributions of two preformed particles.

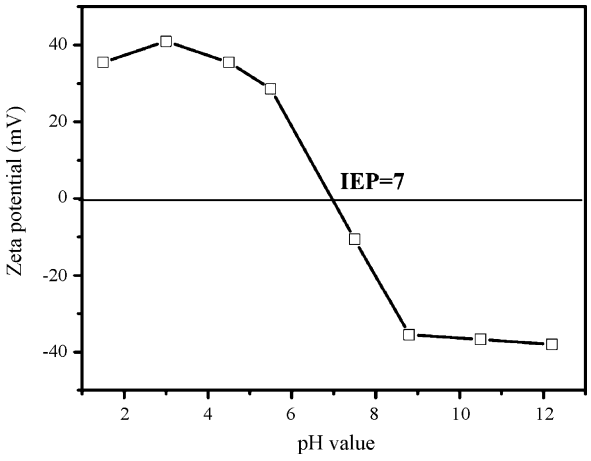

Fig. 6. Zeta potential of nano-particles in water as a function of pH value.

The mechanical properties of coatings were measured using both nano-indentation (nano-indenter® XP, MTS systems corporation, Eden Priarie, Minnesota, USA) and micro-indentation (Wilson Tukon 2100 Indentation Hardness tester, Wilson Instruments, Norwood, USA). Two positions were chosen for characterization, i.e. one is 30–60 μm away from the coating surface (top layer) and the other is 30–60 μm away from the coating–substrate interface (bottom layer). The nano-indenter was positioned on preformed particles which could be clearly seen using an optical microscope under a magnification of 500× (Fig. 3a), and a maximum indentation depth in the range of 1000–2000 nm was used. The micro-indentation was carried out with an applied load of 4.9 N and dwelling time of 10 s. The micro-indenter was observed to cover both preformed particles and nano-particles (Fig. 3b). For both nano-indentation and micro-indentation, the results were averaged out of 15 independent measurements.

3. Results

3.1. Characterization of preformed particles and nano-slurries

SEM examination shows that the irregularly shaped preformed particles remain separated (Fig. 4a) and have been sintered to a full density with a crystallite size of about 150 nm (Fig. 4b). Fig. 5 shows the particle size distributions of the two preformed particles. The average particle size was determined as 24 and 62 μm.

Fig. 6 shows the zeta potential of YSZ nano-particles as a function of pH value. The isoelectrical point (IEP) was determined as 7, similar to the IEP values of various YSZ powders reported in literature.[16,17] When the pH value was adjusted away from 7, the absolute zeta potential increased. Fig. 7 shows the viscosity versus shear rate for nano-slurries. For a given volume fraction of nano-particles (5.2 vol%), the viscosity of nano-slurries increased as the pH value was adjusted from 1.5 to 7.5 (Fig. 7a). This was attributed to the comparatively lower zeta potential at a pH value close to the IEP = 7 (Fig. 6). At a pH of 1.5, the viscosity of nano-slurries increased with the solid content, because the attractive van der Waals forces were significant and the electrical double layer thickness was compressed at a higher solid content (Fig. 7b). It should be pointed out that the viscosity of nano-slurries with solid fraction higher than 9.9 vol% is too high to be measured by the facility used in this study. However, results from Fig. 7 indicate that the slurry with pH of 1.5 should be selected for slurry coating process due to its low viscosity.

3.2. Microstructure of porous YSZ coatings

Table 1 summarizes thickness shrinkages and densities of coatings. In both the drying and sintering processes, the coat-

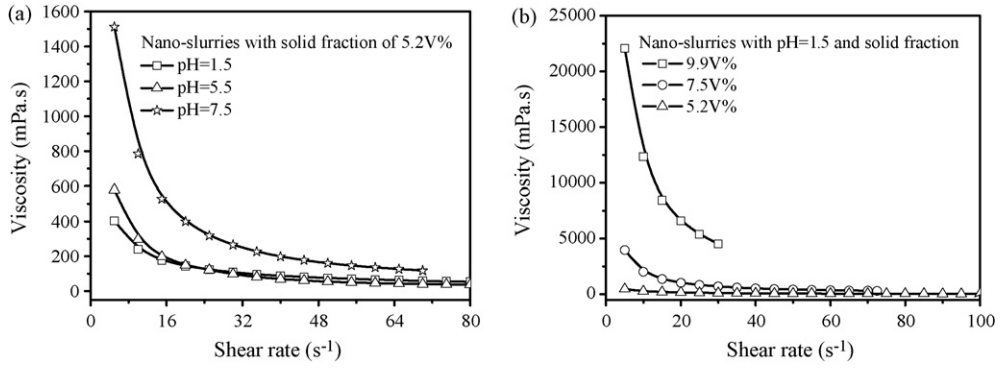

Fig. 7. Viscosity verse shear rate of nano-slurries with different (a) pH values and (b) solid fractions.

Table 1
Thickness shrinkages and densities of YSZ coatings

Preformed particle size (μm)	Drying shrinkage (%)	Green density (g/cm^3)	Sintering shrinkage (%)	Sintered density (g/cm^3)
24	(31 ± 3)	3.5	18.6	4.3
62	(22 ± 3)	3.1	11.4	3.5

ings containing 24 μm preformed particles showed the larger thickness shrinkage and the higher density, in comparison with those containing 62 μm preformed particles. Fig. 8 shows the typical polished and thermally etched cross sections of sintered coatings produced with preformed particles of 24 and 62 μm, respectively. The thickness of both coatings was in the range of 350–420 μm (Fig. 8a and b, insert images). A good bonding was achieved between the coating containing 24 μm particles and substrate via a thin alumina layer which was formed due to oxidation of metal substrates during the coating sintering process (Fig. 8a, insert image). However, crack-like interfacial separation was observed for the coating containing 62 μm preformed particles (Fig. 8b, insert image). It should be noted that observation of the coating/substrate bonding here is not conclusive, and further work is required to confirm the effect of the slurry composition on the bonding. In both coatings, bridging-connections through nano-particles were present between neighboring preformed particles as well as in the coating/substrate interfacial area (Fig. 8a and b). The bridging nanophase showed a porous nanostructure (Fig. 8c) with the presence of micro-sized cracks (Fig. 8b). Fig. 9 shows the typical pore size distributions of sintered coatings. The pore structure data are summarized in Table 2. A trimodal pore size distribution was observed for the two sintered coatings, i.e. sub-micrometer pores <0.1 μm, micro-pores in the range of 0.1–10 μm, and big pores >10 μm. The sintered coating containing 24 μm preformed particles had a lower porosity of 29.4%, in comparison with the 41.9% porosity of the coating containing the 62 μm preformed particles.

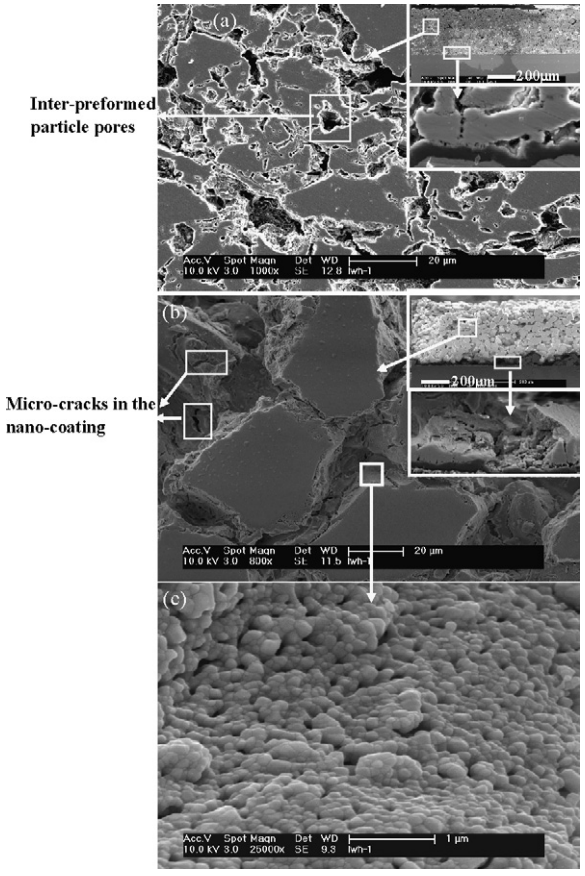

Fig. 8. SEM micrographs of polished and thermally etched cross sections of sintered coatings containing (a) 24 μm and (b) 62 μm preformed particles. (c) The nanostructure between neighboring preformed particles.

3.3. Microstructure of infiltrated YSZ coatings

Figs. 10 and 11 show the relative weight gain for the coating containing 24 μm particles after 1 infiltration cycle as a function of the pH and solid fraction of the infiltrated nano-slurries. When the volume fraction of nano-particles in the slurries was initially controlled at 7.5 vol%, with increased pH from 1.5 to 7.5, the relative weight gain decreased significantly. When the pH was initially adjusted at pH 1.5, with an increase in the solid fraction, the relative weight gain increased first, reached a maximum for the nano-slurry with an 11.5 vol% solid fraction, and then decreased with a further increase in the solid fraction to 18.6 vol%.

In view of the most efficient infiltration with the nano-slurry with pH 1.5 and 11.5 vol% solid fraction (Figs. 10 and 11), this slurry was chosen for multicycle infiltration. For both coatings, with an increase in the number of infiltration cycles, the accumulative weight gain increased, whereas the relative weight gain of each cycle reduced (Fig. 12). After a given infiltration cycle, a higher relative weight gain was obtained

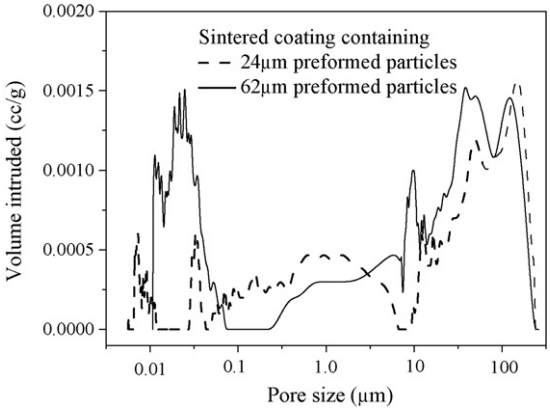

Fig. 9. Pore size distributions of sintered coatings.

Table 2
Pore structure data of sintered YSZ coatings

Preformed particle size (μm)	Pore volume in 1 g coating (cm^3)	Calculated porosity[#] (%)	Volume of pores < 0.1 μm (cm^3)	Volume of 0.1 μm < pores < 10 μm (cm^3)	Volume of pores > 10 μm (cm^3)
24	0.0688	29.4	0.0279	0.0111	0.0298
62	0. 1190	41.9	0.0651	0.015	0.0389

[#] Porosity is calculated by (pore volume/(pore volume + solid volume), solid volume = 1/6.05).

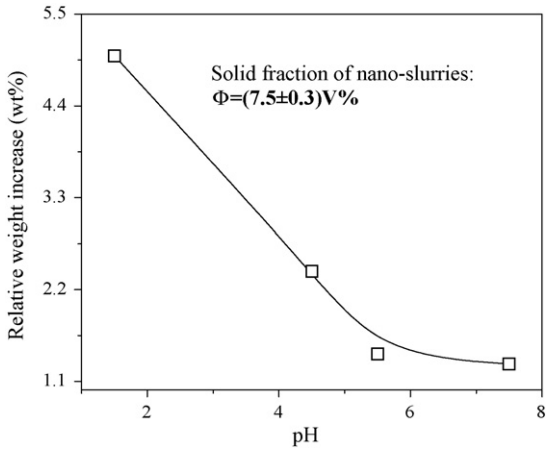

Fig. 10. Relative weight gain after 1 infiltration cycle as a function of the pH of infiltrated nano-slurries which had constant solid fraction of 7.5 vol%.

for the coating containing larger preformed particles or higher porosity. When the relative weight gain after an infiltration cycle was lower than 1 wt%, the coatings were defined as saturation-infiltrated coatings. The densities of infiltrated coating were calculated using Eq. (3) and are summarized in Table 3. A relatively high density of 5.0 g/cm^3 (82% theoretical density) has been achieved for the saturation-infiltrated coatings containing 24 μm preformed particles after 5 infiltration cycles.

Figs. 13 and 14 show SEM micrographs of the cross sections of infiltrated coatings as a function of infiltration cycles. With an increase in the number of infiltration cycles, the interstices between preformed particles became narrow, and nearly closed up for the saturation-infiltrated coatings (Figs. 13c and 14c). Meanwhile, the individual preformed particles seemed to grow bigger with an increase in the number of infiltration cycles. After infiltration, a gradient microstructure was observed with a top dense layer and a bottom porous layer (Fig. 15). Such a structural feature is desirable for the application as thermal barrier coatings (TBCs).[18] During service, the denser top layer can ensure the coating strength to resist mechanical damage and corrosion, whereas, the porous bottom layer can help with the thermal mismatch between the ceramic coating and the metal substrate.

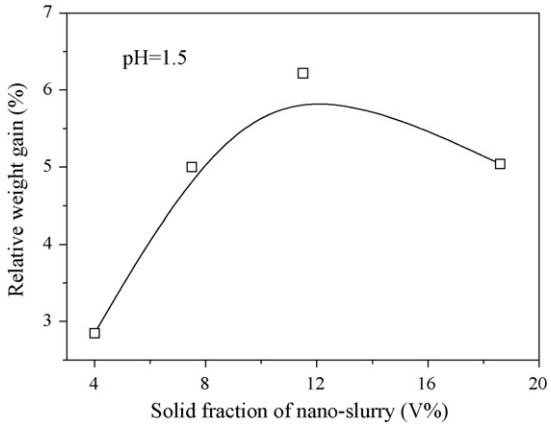

Fig. 11. Relative weight gain after 1 infiltration cycle as a function of the solid fraction of the infiltrated nano-slurries with pH of 1.5.

3.4. Mechanical properties of YSZ coatings

Fig. 16 shows the Young's modulus as a function of average coating density, measured by carrying out nano-indentation on preformed particles with the maximum indentation depths in the range of 1000–2000 nm. The coating density is the average density calculated using Eq. (3). In general, as the density increased with infiltration cycles (Table 3), the Young's modulus increased. Comparison between Fig. 16(a and b), at the same density of 4.7 g/cm^3, showed that the measured Young's modulus of the coating containing 62 μm particles was slightly higher than that of the coating containing 24 μm particles. For both coatings, the Young's modulus became lower with increasing indentation depth from 1000 to 2000 nm. With indentation at a given depth, the measured Young's modulus of a top layer was slightly higher than that of a corresponding bottom layer. The difference of the Young's modulus between these two positions became more obvious with the increased indentation depth. Fig. 17 shows the micro-hardness measured using micro-indentation as a func-

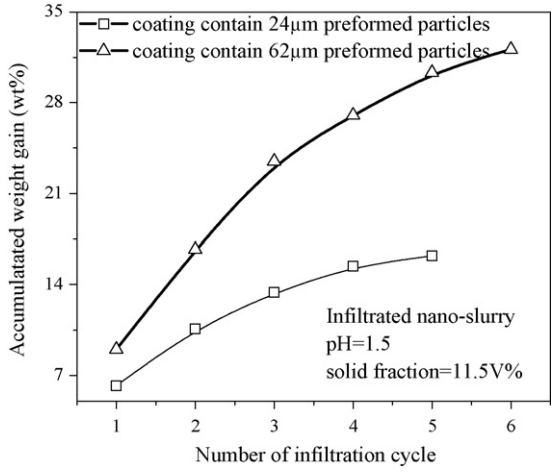

Fig. 12. Accumulative weight gain as a function of infiltration cycles for coatings containing different preformed particles. The infiltrated nano-slurry has pH 1.5 and a solid fraction of 11.5 vol%.

Table 3
Coating density as a function of infiltration cycles

Infiltration cycles (μm)	0 (g/cm^3)	1 (g/cm^3)	2 (g/cm^3)	3 (g/cm^3)	4 (g/cm^3)	5 (g/cm^3)	6 (g/cm^3)
24*	4.3	4.5	4.7	4.8	4.9	5.0	
62*	3.5	3.8	4.1	4.4	4.5	4.6	4.7

The infiltrant nano-slurry is with a pH 1.5 and solid fraction of 11.5 vol%.

* Coatings containing 24 μm or 62 μm preformed particles.

tion of coating density. Consistent with the measurement of nano-indentation (Fig. 16), the micro-hardness increased with density, the top layer had a higher micro-hardness than the bottom layer.

4. Discussion

4.1. Sintering of porous YSZ coatings

Since the preformed particles are almost fully dense (Fig. 4) and separated from each other by nano-particles, the densification of coatings is mainly contributed by the densification of nano-particles. Preformed particles are treated as substrates on which nano-particles are present and sintered. By analogy with the constrained sintering of thin films on rigid substrates,[19,20] local tensile stresses developed when the nano-particles sintered under the constraint from the preformed particles, resulting in a porous nano-structure and the formation of micro-sized cracks (Fig. 8b and c). The inter-preformed particle space controls the thickness of the 'nano-particle coating' on the preformed particles. For a given preformed/nano-particle ratio of 5, the larger the preform particle, the thicker is the nano-particle coating. Micro-cracks are more likely to be in the thicker 'nano-particle coating' on larger preformed particles, i.e. the coating containing 62 μm preformed particles (Fig. 8b). As nanocrystalline YSZ exhibits superplasticity at high temperature,[21,22] the nano-particles present between preformed particles could be stretched, compressed and twisted without breaking the continuity of the inter-preformed particle links (Fig. 8), which is crucial for application of the 'mortar-bricks' approach.

Fig. 9 shows trimodal pore size distributions for the two coatings with pore size distribution of pores <0.1 μm, 0.1 μm < pores < 10 μm and pores > 10 μm. According to SEM observations, both nano-pores (Fig. 8c) and crack-like defects (Fig. 8b) in the nano-coating region are of sub-micrometer size, which may contribute to the first-order pores (<0.1 μm) in Fig. 9. In a previous paper,[7] it was observed that preformed particles in a matrix of the nano-slurry rearranged their positions during the early drying stage and then the movement of preformed particles stopped in the later drying stage, where localized contraction of the nano-slurry around the preformed particles induced cracks or pores between preformed particles, as schematically shown in Fig. 18. These pores were referred to as inter-preformed particle-pores which could increase when the

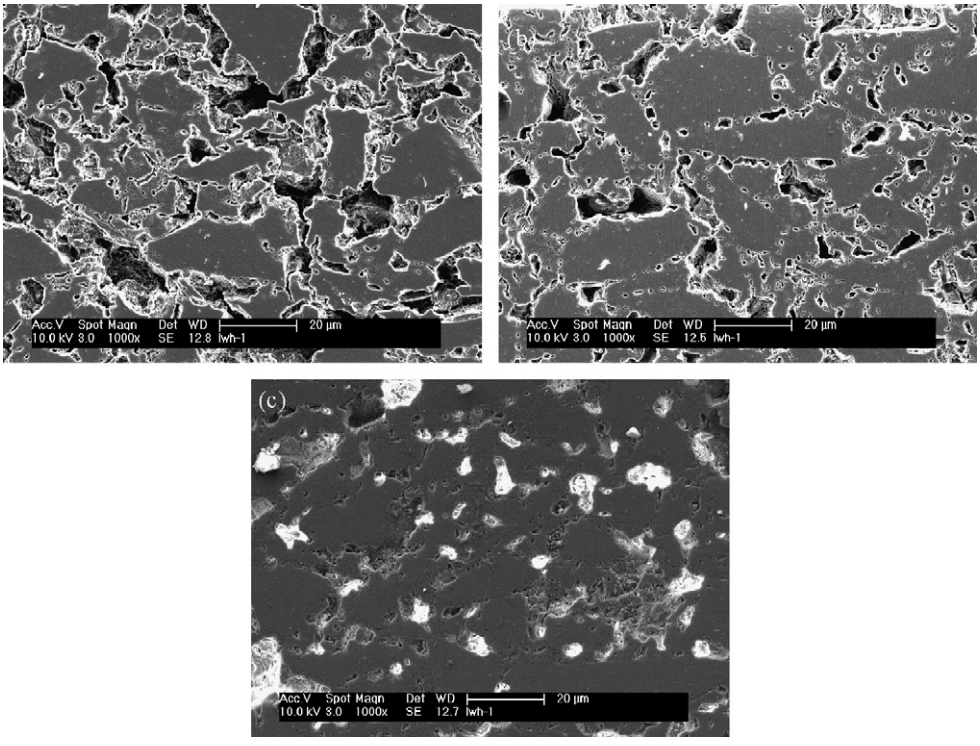

Fig. 13. SEM micrographs of the cross sections of the sintered coatings containing 24 μm preformed particles with (a) 0, (b) 3 and (c) 5 infiltration cycles.

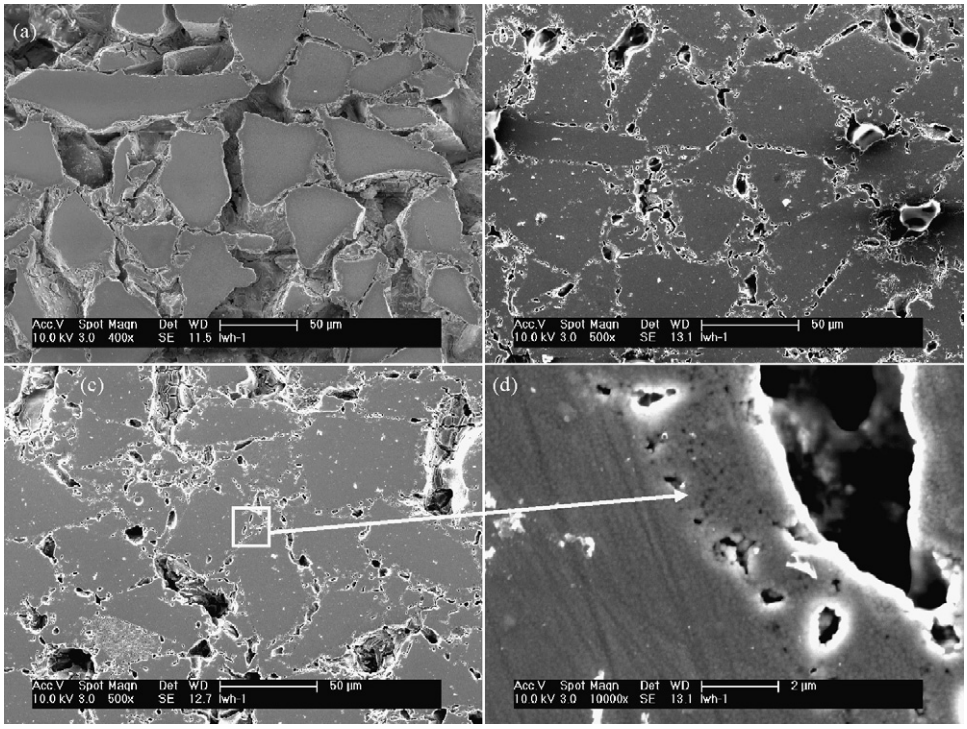

Fig. 14. SEM micrographs of the cross sections of the sintered coatings containing 62 μm preformed particles with (a) 0, (b) 3, (c) 6 infiltration cycles and (d) magnified image of connection between nanophase and preformed particles.

nano-coating continued to shrink during sintering. It is believed that these inter-preformed particle pores which have a size comparable to the preformed particles contributed to the second-order pores (0.1 μm < pores < 10 μm) in Fig. 9. Fig. 8 shows that inter-preformed particle pores are connected by micro-cracks which are formed in the nano-coating (Fig. 18). These interconnected pores may contribute to the third-order pores (10 μm < pores < 200 μm) in Fig. 9. The interconnected pores provide a flow path for infiltrated nano-slurries, which will be discussed in the next section.

4.2. Infiltration dynamics

Figs. 13 and 14 indicate that the nano-slurry was infiltrated into the inter-preformed particle pores, and consolidated on the previous pore walls (Fig. 14d). According to the Darcy's law,[23]

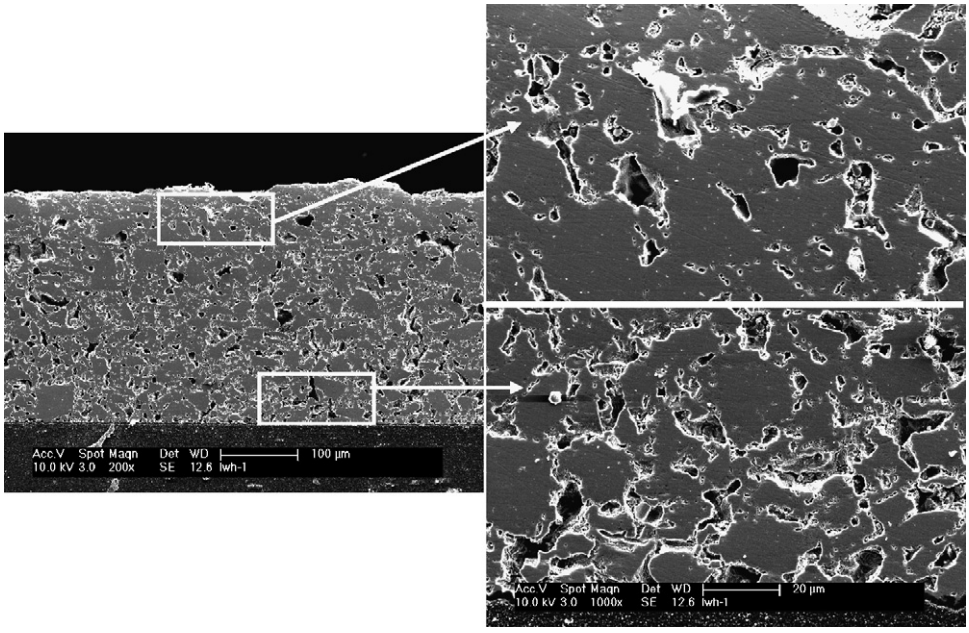

Fig. 15. SEM micrograph of the cross section of a coating containing 24 μm preformed particles after 4 infiltration cycles.

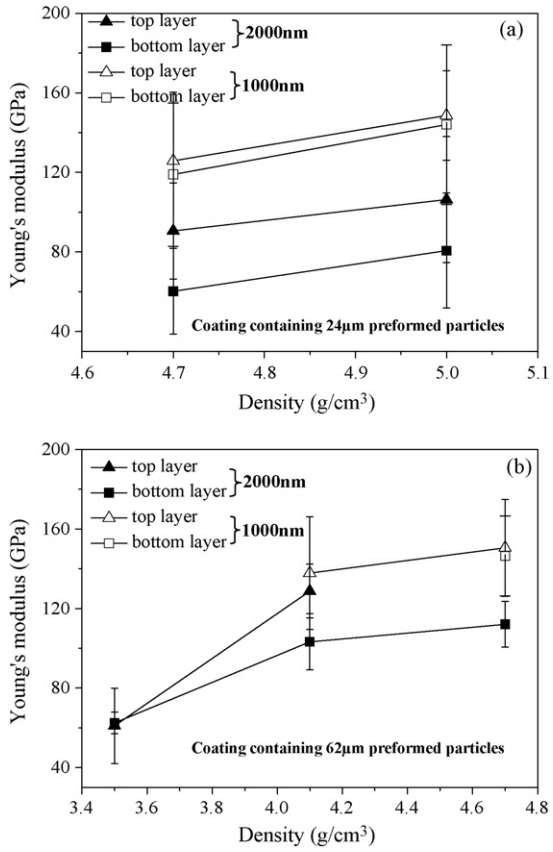

Fig. 16. Young's modulus as a function of density measured by carrying out nano-indentation on preformed particles with different indentation depths.

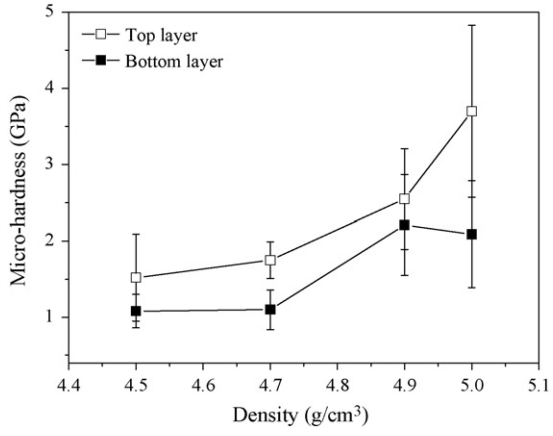

Fig. 17. Micro-hardness as a function of density of coatings containing 24 μm preformed particles.

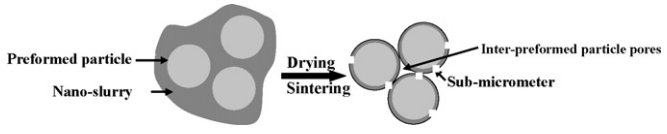

Fig. 18. Formation of cracks/pores in coatings containing preformed particles during drying and sintering.

the flow rate of a nano-slurry within a porous coating, v_w, could be written as:

$$v_w = -\frac{\kappa_w}{\mu}\frac{dP}{dh} \tag{4}$$

where κ_w is the effective permeability of a porous coating, μ is the viscosity of a nano-slurry, and dP/dh is the pressure gradient driving the slurry flow. The volume of the infiltrated nano-slurry, V, under an applied pressure, P (100 MPa), should be approximated by:

$$V \propto v_w A \propto -\frac{\kappa_w PA}{\mu h} \tag{5}$$

where A is the coating surface area, and h is the sintered coating thickness which is in the range of 350–420 μm (Fig. 8a and b, insert images) and is treated as a constant in this study. After water evaporation of the infiltrated nano-slurry, the relative weight gain, $W\%$, after an infiltration cycle should be:

$$W\% \propto -\frac{\phi\kappa_w PA\rho}{\mu W_I} \tag{6}$$

where ϕ is the volume fraction of nano-particles in an infiltrated nano-slurry, ρ is the theoretical density of YSZ particles taken as 6.05 g/cm^3, and W_I is the initial weight of the sintered coating without any infiltration.

Eq. (6) indicates that the relative weight gain after an infiltration cycle is dependent on both the slurry properties, i.e. the volume fraction of nano-particles (ϕ), the viscosity (μ), and the permeability of sintered coatings (κ_w), which is consistent with the experimental results. For infiltration in a porous coating with nano-slurries with a fixed solid content of 5.2 vol% and different pH values, $(-\kappa_w PA\rho/W_I)$ was constant to be recorded as K_1, and the relative weight gain was inversely proportional to the viscosity of the infiltrated nano-slurry, μ (Eq. (7), Fig. 10).

$$W\% \propto \frac{K_1}{\mu} \tag{7}$$

For infiltration in a porous coating with slurries containing different solid fractions, $(-\kappa_w PA\rho/W_I)$ was constant to be recorded as K_2, and the relative weight gain was a function of two factors, i.e. the viscosity (μ) and solid fraction (ϕ) of the infiltrated nano-slurry (Eq. (8)).

$$W\% \propto \frac{K_2\phi}{\mu} \tag{8}$$

According to the Krieger–Dougherty equation,[24] the slurry viscosity is related to the volume fraction of particles by:

$$\frac{\mu}{\mu_s} = \left(1 - \frac{\phi}{\phi_m}\right)^{-[\eta]\phi_m} \tag{9}$$

where μ_s is the viscosity of the solvent, ϕ_m is the maximum particle packing fraction taken as 0.67 for soft-sphere systems,[25] and $[\eta]$ is the intrinsic viscosity taken as 2.5 for spherical particles. Substituting μ from Eq. (9), Eq. (8) can be rewritten as:

$$W\% \propto K_2\phi\left(1 - \frac{\phi}{0.67}\right)^{1.675} \tag{10}$$

It was calculated that when $\phi = 24$ vol%, W% reached a maximum. However, the experimental results showed that W% reached a maximum when $\phi = 11.5$ vol%, which was much lower than the calculated value of 24 vol%. The difference might be caused by two reasons. In the nano-slurry with pH 1.5, the repulsive electrical double-layers are adsorbed on the nano-particle surfaces and occupy a volume, which increases the effective volume fraction of particles by:[26]

$$\phi_{\text{eff}} = \phi\left(1 + \frac{\delta}{R_{\text{P}}}\right)^3 \tag{11}$$

where δ is the thickness of the repulsive electrical double-layer, and R_{P} is the particle radius. In addition, water evaporation during vacuuming also led to under-estimation of the solid fraction for the optimal infiltration.

Eq. (6) also predicts that the relative weight gain is inversely proportional to the permeability of a coating which is related to the pore structure. Table 3 shows a larger volume of inter-connective micro-pores (pores > 10 μm) which provide the infiltration path and represent a higher permeability for the coatings containing 62 μm preformed particles. In addition, infiltration of nano-slurries diminished pores and reduced the permeability of coatings (Figs. 13 and 14). Therefore, the relative weight gain of each cycle was higher in the coating containing 62 μm preformed particles than that containing 24 μm preformed particles, and decreased with an increase in the number of infiltration cycles (Fig. 12).

4.3. Mechanical properties of coatings

Fig. 4(b) shows that preformed particles have been sintered to almost fully dense. Taking into consideration the preparation procedure of preformed particles, the mechanical properties of an individual preformed particle should be equal or close to those of a fully dense YSZ from sintering of the nano-particle compact, of which the Young's modulus was measured as (244 ± 14) GPa in this study. However, the Young's modulus obtained from nano-indentation of preformed particles in the coatings gave the much lower Young's modulus than 244 GPa (Fig. 16). That is because the preformed particles were bridged with porous nano-particle network (Fig. 8), which gave soft substrate effect.[27] The difference between measured Young's modulus and 244 GPa reflects the porosity level in the bridging nanophase. A dense bridging nanophase with a high mechanical strength is crucial to ensure the coating integrity. In addition, the difference is dependent on the ratio of indentation depth to preformed particle size, $h_{\text{indentation}}/D_{\text{particle}}$. The higher the ratio of $h_{\text{indentation}}/D_{\text{particle}}$, the more mechanical information is taken from the nano-particles underneath. A higher Young's modulus was measured when nano-indentation was carried out on larger preformed particles or with a lower indentation depth (Fig. 16). The Young's modulus increased with density, which increased with infiltration cycles.

For micro-indentation measurements, the micro-indenter covered both preformed particles and nano-particles (Fig. 3b), and the micro-hardness represented the overall mechanical properties of coatings which were also improved by infiltration (Fig. 17). An increase in the micro-hardness towards the coating surface is resulted from a decrease of the porosity during infiltration (Figs. 15 and 17).

5. Conclusions

(1) By adopting the 'mortar-bricks' approach, YSZ coatings with thicknesses up to 420 μm have been fabricated. After sintering at 1150 °C for 1 h, preformed particles and the metal substrate were cemented by nano-particles, leaving micro-sized pores or cracks between preformed particles which were interconnected.

(2) A nano-slurry has been infiltrated into a porous sintered coating through the interconnected pores between preformed particles under an applied pressure. The infiltrated ceramic particles were sintered onto the pore walls and blocked the pores of the coating eventually, resulting in an increase in both packing density and mechanical properties. A relatively high density of 5 g/cm^3 has been achieved for coatings with saturated infiltration.

(3) The infiltration is dependent on both the viscosity of nano-slurries and the microstructure of sintered coatings. The interconnected pores between preformed particles provided the pathway for the infiltrated nano-slurry. Both a lower viscosity and a lower drying shrinkage of nano-slurries were desirable for infiltration. The optimal nano-slurry used for infiltration was found to be with a pH 1.5 and 11.5 vol% solid content.

(4) A gradient microstructure with a denser top layer and a more porous bottom layer was obtained after infiltration, which was desirable for an application as thermal barrier coatings.

Acknowledgement

Mel Chemicals is acknowledged for providing YSZ slurry.

References

1. Chiu, R. C., Garino, T. J. and Cima, M. J., Drying of granular ceramic films: I. Effect of processing variables on cracking behaviour. *J. Am. Ceram. Soc.*, 1993, **76**(9), 2257–2264.
2. Lewis, J. A., Blackman, K. A., Ogden, A. L., Payne, J. A. and Francies, L. F., Rheological properties and stress development during drying of tape-cast ceramic layers. *J. Am. Ceram. Soc.*, 1996, **79**(12), 3225–3234.
3. Stech, M., Reynder, P. and Rodel, J., Constrained film sintering of nanocrystalline TiO_2. *J. Am. Ceram. Soc.*, 2000, **83**(8), 1889–1896.
4. Lu, G. Q., Sutterlin, R. C. and Gupta, T. K., Effect of mismatched sintering kinetics on camber in a low-temperature cofired ceramic package. *J. Am. Ceram. Soc.*, 1993, **76**(8), 1907–1914.
5. Lan, W. H., Wang, X. and Xiao, P., Agglomeration effect on drying of yttria-stabilized-zirconia slurry on a metal substrate. *J. Eur. Ceram. Soc.*, 2006, **26**(16), 3599–3606.
6. Lan, W. H. and Xiao, P., Drying stress of yttria-stabilized-zirconia slurry on metal substrate. *J. Eur. Ceram. Soc.*, 2007, **27**, 3117–3125.

7. Lan, W. H. and Xiao, P., Constrained drying behaviour of yttira-stabilized-zirconia slurry on a substrate: II. Binary particle slurries. *J. Am. Ceram. Soc.*, 2007, **90**, 2771–2778.
8. Garino, T. J. and Bowen, H. K., Deposition and sintering of particle films on a rigid substrate. *J. Am. Ceram. Soc.*, 1987, **70**(11), C315–C317.
9. Herring, C., Diffusional viscosity of a polycrystalline solid. *J. Appl. Phys.*, 1950, **21**(5), 437–445.
10. Raj, R., Analysis of the sintering pressure. *J. Am. Ceram. Soc.*, 1987, **70**(9), C210–C211.
11. Wang, X., Lan, W. H. and Xiao, P., Fabrication of yttria stabilized zirconia coatings by a novel slurry method. *Thin Solid Films*, 2006, **494**(1/2), 263–267.
12. Lange, F. F. and Miller, K. T., Pressure filtration: consolidation kinetics and mechanics. *Am. Ceram. Soc. Bull.*, 1987, **66**(10), 1498–1507.
13. Qi, G. J., Zhang, C. R., Hu, H. F., Cao, F., Wang, S. Q., Cao, Y. B. *et al.*, Preparation of three dimensional silica fiber reinforced silicon nitride composite using perhydropolysilazane as precursor. *Mater. Lett.*, 2005, **59**, 3256–3258.
14. Dey, A., Chatterjee, M., Naskar, M. K. and Basu, K., Near-net-shape fibre-reinforced ceramic matrix composites by the sol infiltration technique. *Mater. Lett.*, 2003, **57**, 2919–2926.
15. Rak, Z. S., A Process for C_f/SiC composites using liquid polymer infiltration. *J. Am. Ceram. Soc.*, 2001, **84**(10), 2235–2239.
16. Agrafiotis, C., Tsetsekou, A. and Leon, I., Effect of slurry rheological properties on the coating of ceramic honeycombs with yttria-stabilised-zirconia washcoats. *J. Am. Ceram. Soc.*, 2000, **83**(5), 1033–1038.
17. Wang, Y. H., Liu, X. Q. and Meng, G. Y., Dispersion and stability of 8 mol% yttria stabilized zirconia suspensions for dip-coating filtration membranes. *Ceram. Int.*, 2007, **33**(6), 1025–1031.
18. Portinha, A., Teixeira, V., Carneiro, J., Martins, J., Costa, M. F., Vassen, R. *et al.*, Characterization of thermal barrier coatings with a gradient in porosity. *Surf. Coat. Technol.*, 2005, **2195**(2/3), 245–251.
19. Bordia, R. K. and Raj, R., Sintering behaviour of ceramic films constrained by a rigid substrate. *J. Am. Ceram. Soc.*, 1985, **68**(6), 287–292.
20. Guillon, O., Krau, S. and Rodel, J., Influence of thickness on the constrained sintering of alumina films. *J. Eur. Ceram. Soc.*, 2007, **27**, 2623–2627.
21. Mayo, M. J., Seidensticker, J. R., Hague, D. C. and Carim, A. H., Surface chemistry effects on the processing and superplastic properties of nanocrystalline oxide ceramics. *NanoStruct. Mater.*, 1999, **11**, 271–282.
22. Jimenez-Melendo, M., Dominguez-Rodriguez, A. and Bravo-Leon, A., Superplastic flow of fine grained yttria-stabilised zirconia polycrystals: constitutive equation and deformation mechanisms. *J. Am. Ceram. Soc.*, 1998, **81**(11), 2761–2776.
23. Dullien, F. A. L., *Porous Media: Fluid Transport and Pore Structure*. Academic Press, New York, 1979 [Chapter 4].
24. Krieger, I. M. and Dougherty, T. J., A mechanism for non-newtonian flow in suspensions of rigid spheres. *Trans. Soc. Rheol.*, 1959, **3**, 137–152.
25. Ferreira, J. M. F. and Diz, H. M. M., Effect of solid loading on slip casting performance of silicon carbide slurries. *J. Am. Ceram. Soc.*, 1999, **82**(8), 1993–2000.
26. Bergstrom, L., Schilling, C. H. and Aksay, I. A., Consolidation behaviour of flocculated alumina suspensions. *J. Am. Ceram. Soc.*, 1992, **75**(12), 3305–3314.
27. Saha, R. and Nix, W. D., Effects of the substrate on the determination of thin film mechanical properties by nanoindentation. *Acta Mater.*, 2002, **50**, 23–28.